High Resolution Algorithms for Multidimensional Population Balance Equations

Rudiyanto Gunawan, Irene Fusman, and Richard D. Braatz
Dept. of Chemical and Biomolecular Engineering, University of Illinois, Urbana, IL 61801

DOI 10.1002/aic.10228
Published online in Wiley InterScience (www.interscience.wiley.com).

Population balance equations have been used to model a wide range of processes including polymerization, crystallization, cloud formation, and cell dynamics. Rather than developing new algorithms specific to population balance equations, it is proposed to adapt the high-resolution finite volume methods developed for compressible gas dynamics, which have been applied to aerodynamics, astrophysics, detonation waves, and related fields where shock waves occur. High-resolution algorithms are presented for simulating multidimensional population balance equations with nucleation and size-dependent growth rates. For sharp distributions, these high-resolution algorithms can achieve improved numerical accuracy with orders-of-magnitude lower computational cost than other finite difference and finite volume algorithms. The algorithms are implemented in the ParticleSolver software package, which is applied to batch and continuous processes with one and multiple internal coordinates. © 2004 American Institute of Chemical Engineers *AIChE J,* 50: 2738–2749, 2004

Keywords: population balance equations, distributed parameter systems, finite volume methods, numerical analysis, hyperbolic equations, crystallization

Introduction

Many chemical processes, including polymerization, solution crystallization, cloud formation, and cell dynamics, are best described by population balance equations (Ramkrishna, 2000). Consider the one-dimensional (1-D) population balance equation

$$\frac{\partial f(L,\,t)}{\partial t} + \frac{\partial\{G(L,\,t)\,f(L,\,t)\}}{\partial L} = h(L,\,t,\,f) \qquad (1)$$

where $f(L,\ t)$ is the distribution (also called the population density), t denotes the time, L is an internal coordinate, $G(L,\ t)$ is the growth/dissolution rate, and $h(L,\ t,\ f)$ is the creation/depletion rate. The entities in the distribution can be molecules, cells, crystals, cloud particles, amorphous globs, and so on. The internal coordinate L, often referred to as the size, is typically the characteristic length, volume, or mass, but it can also represent age, composition, and other characteristics of an entity in a distribution. The creation/depletion rate $h(L,\ t,\ f)$ includes nucleation, aggregation, agglomeration, breakage, attrition, and material leaving or entering the system, and can be a function of other variables including the distribution, which occurs in nucleation processes resulting from particle-particle interactions and in agglomeration processes. Many of these expressions involve integrals so that Eq. 1 is typically an integrodifferential equation. The growth/dissolution rate $G(L,\ t)$ can be a function of size and other variables, such as the temperature and the concentration of chemical species in solution. The growth/dissolution and creation/depletion rates are typically highly nonlinear functions of their arguments.

An accurate simulation of the distribution can be challenging in that the distribution can extend many orders of magnitude in size and time, and changes in the distribution can be very sharp. This has motivated many researchers to develop specialized algorithms for solving population balance equations (for example, see Ramkrishna, 1985; Nicmanis and Hounslow, 1998; Ramkrishna, 2000, and citations therein). These methods can

Correspondence concerning this article should be addressed to R. D. Braatz at braatz@uiuc.edu.

be roughly divided into five categories: the method of moments, the method of characteristics, the method of weighted residuals/orthogonal collocation, Monte Carlo simulation, and finite difference methods/discretized population balances. The method of moments approximates the distribution by its moments (Hulburt and Katz, 1964). Under certain conditions, the moment equations are closed, that is, the differential equations for the lower order moments do not depend on values for the higher-order moments, which results in a small number of ordinary differential equations (ODEs) that can be solved very efficiently and with very high accuracy using off-the-shelf ODE solvers. The main weakness of the method of moments is the moment closure conditions are violated for more complex systems. The method of characteristics aims to solve the population balance equation by finding curves in the *L-t* plane that reduce the equation to an ODE. While the method is highly efficient when the physics are simple, the approach does not generalize to complex physics. The method of weighted residuals approximates the distribution by a linear combination of basis functions (Singh and Ramkrishna, 1977). As in the method of moments, this results in a system of ODEs, which can be solved using off-the-shelf solvers. The main weakness of this approach is that the basis functions must be carefully tuned to each specific system if a small number of ODEs is desired. Monte Carlo simulations track the histories of individual particles, each of which exhibits random behavior according to a probabilistic model (Shah et al., 1977; Maisels et al., 1999; Song and Qiu, 1999). Monte Carlo simulations are most suitable for stochastic population balance equations, especially for complex systems (Ramkrishna, 1985). This method is typically computationally expensive. In the method of finite differences/discretized population balances, the population balance equation is approximated by a finite difference scheme (Kumar and Ramkrishna, 1996). Numerous discretizations of the PBE with different orders of accuracy have been investigated and applied to various particulate systems (Gelbard et al., 1980; Hounslow et al., 1988; Marchal et al., 1988; Hounslow, 1990; Muhr et al., 1996; Kumar and Ramkrishna, 1997).

An alternative approach was recently proposed (Ma et al., 2002), which is to apply the high resolution finite volume methods developed for compressible gas dynamics, which are the state-of-the-art methods in aerodynamics, astrophysics, detonation waves, and related fields where shock waves occur (LeVeque et al., 1998). The high-resolution algorithms have been specifically developed to provide high accuracy while avoiding the numerical diffusion (that is, smearing) and numerical dispersion (that is, nonphysical oscillations) associated with other finite difference and finite volume methods. This approach adapts the state-of-the-art methods used by researchers to simulate the most challenging hyperbolic equations, to gain from their experience and efforts, rather than developing new algorithms specific to population balance equations. An advantage of this approach is that many of the high-resolution algorithms developed in compressible gas dynamics, including the algorithms investigated here, are general purpose. This allows the simulation code to be quickly modified by a nonexpert to solve a particular problem of interest.

A recent book (LeVeque, 2002) extended high-resolution algorithms to the simulation of variable-coefficient linear hyperbolic systems. These systems have the same mathematical structure as the population balance equations with size-dependent growth and, thus, the high-resolution algorithms directly apply to these equations. In addition, this article shows how to transform the size-dependent population balance equation so that the high-resolution algorithm for constant growth in (Ma et al., 2002) also applies to such PBEs. The algorithms can provide second-order accuracy for all regions in which the solution is smooth, and avoid the numerical diffusion associated with first-order methods, and the numerical dispersion near discontinuities or sharp gradients associated with other second-order methods. The high-resolution algorithms are compared to two popular methods for solving population balance equations, in simulations of several batch and continuous population balance models with one or two internal coordinates, and a variety of initial conditions.

High Resolution Finite Volume Algorithms

This section briefly reviews high resolution finite volume methods, followed by a presentation of the high-resolution algorithms for handling size-dependent growth and comments on multidimensional population balance equations and implementation.

High-resolution methods were developed for solving the nonlinear hyperbolic equation (LeVeque et al., 1998)

$$\frac{\partial u(x, t)}{\partial t} + \frac{\partial}{\partial x} F(u) = 0 \tag{2}$$

where x and u denote the spatial and state variables, respectively. This hyperbolic equation is common in applications as it arises naturally in material, energy, and momentum balances. Analytical solutions are not possible except for a limited number of simple problems, which is why much effort has been invested in computational fluid dynamics and related areas to numerically simulate these equations. Numerical difficulties can arise for problems with discontinuities or where the spatial derivative in Eq. 2 is very large. First-order methods tend to produce numerical diffusion, where the solution is smeared or damped and most second-order methods can produce numerical dispersion, which is the appearance of nonphysical oscillations (Morton and Mayers, 1994). The term "high-resolution method" refers to a numerical algorithm that is designed to provide at least second-order accuracy where the solution is smooth, and that does not introduce numerical dispersion (LeVeque et al., 1998). Modern high-resolution methods are derived from an integral representation for the underlying conservation equations, and so are in the class of finite volume methods. This ensures that the main property of the distribution (for example, total material, total energy, total momentum) is exactly conserved, as well as ensuring accurate simulation of growth rate kinetics (LeVeque et al., 1998), without requiring specialized procedures as typically required by finite difference methods.

The presentation will summarize the homogeneous 1-D case first, followed by the extension to nonhomogeneous higher dimensional systems. Let k and h denote the time and size intervals, respectively, and f_n^m denote an approximation of the average population density

$$f_n^m \approx \frac{1}{\Delta x}\int_{(n-1)h}^{nh} f(x, mk)dx \tag{3}$$

where m, n are integers such that $m \geq 0$ and $1 \leq n \leq N$.

Size-independent growth

The homogeneous population balance equation with size-independent growth is

$$\frac{\partial f}{\partial t} + g\,\frac{\partial f}{\partial L} = 0 \tag{4}$$

with the initial distribution $f(L, 0)$, and the constant growth rate g. Assuming $g > 0$ (a similar derivation holds for $g < 0$), a class of high resolution finite volume algorithms that is second-order accurate almost everywhere has the form (LeVeque et al., 1998)

$$f_n^{m+1} = f_n^m - \frac{kg}{h}\,(f_n^m - f_{n-1}^m) - \frac{kg}{2h}\left(1 - \frac{kg}{h}\right) \times [(f_{n+1}^m - f_n^m)\phi_n - (f_n^m - f_{n-1}^m)\phi_{n-1}] \tag{5}$$

where the flux limiter function $\phi_n = \phi(\theta_n)$ depends on the degree of smoothness of the distribution, which is quantified by the ratio of two consecutive gradients

$$\theta_n = \frac{f_n^m - f_{n-1}^m}{f_{n+1}^m - f_n^m} \tag{6}$$

The following conditions ensure second-order accuracy wherever the solution is smooth (LeVeque, 1992)

$$\begin{aligned} &1.\quad \phi(\theta) \text{ is bounded with } \phi(1) = 1 \\ &\quad\ \text{and } \phi \text{ is Lipshitz continuous at } \theta = 1 \\ &2.\quad 0 \leq \frac{\phi(\theta_n)}{\theta_n} \leq 2 \ \ \forall\, n \\ &3.\quad 0 \leq \phi(\theta_n) \leq 2 \ \ \forall\, n \end{aligned} \tag{7}$$

Many flux limiter functions have been proposed, including the minmod, superbee, MC, and van Leer (LeVeque et al., 1998). Each flux limiter leads to a different high-resolution method. The MC and Van Leer limiters provide full second-order accuracy. We have had good experience with the Van Leer flux limiter (van Leer, 1974)

$$\phi(\theta_n) = \frac{|\theta_n| + \theta_n}{1 + |\theta_n|} \tag{8}$$

For 1-D problems, this method is *total variation diminishing*, which implies that the algorithm will not introduce numerical dispersion (LeVeque et al., 1998).

Size-dependent growth

The homogeneous population balance equation with size-dependent growth is

$$\frac{\partial f}{\partial t} + \frac{\partial (G(L) f)}{\partial L} = 0 \tag{9}$$

with the initial condition $f(L, 0)$ and growth rate $G(L)$. A recent book (LeVeque, 2002) presented two high-resolution methods for simulating such hyperbolic systems, which differ in the selection of the growth rates in the algorithms. The first algorithm HR1 is a formal second-order accurate method when no flux limiter is used. Here, the growth rates are evaluated at the endpoints of each grid cell (LeVeque, 2002)

$$\text{HR1:}\quad f_n^{m+1} = f_n^m - \frac{k}{h}\,(G_n f_n^m - G_{n-1} f_{n-1}^m) - \left[\frac{kG_n}{2h}\left(1 - \frac{kG_n}{h}\right) \times (f_{n+1}^m - f_n^m)\phi_n - \frac{kG_{n-1}}{2h}\left(1 - \frac{kG_{n-1}}{h}\right)(f_n^m - f_{n-1}^m)\phi_{n-1}\right] \tag{10}$$

where $G_n = G(nh)$. The same flux limiter (Eq. 8) can be used to achieve the desired nonoscillatory solution around discontinuities and second-order accuracy in the smooth regions of the solution. Although the second method (HR2) is not formally second-order accurate even without the flux limiter, this method in practice can provide comparable accuracy with the first method. In this method, the growth rates are evaluated at the grid midpoints (LeVeque, 2002)

$$\begin{aligned} \text{HR2:}\quad f_n^{m+1} = f_n^m &- \frac{k}{h}\,(G_{n-1/2} f_n^m - G_{n-3/2} f_{n-1}^m) \\ &- \left[\frac{k}{2h}\left(1 - \frac{kG_{n+1/2}}{h}\right)(G_{n+1/2} f_{n+1}^m - G_{n-1/2} f_n^m)\phi_n \right. \\ &\left. - \frac{k}{2h}\left(1 - \frac{kG_{n-1/2}}{h}\right)(G_{n-1/2} f_n^m - G_{n-3/2} f_{n-1}^m)\phi_{n-1}\right] \end{aligned} \tag{11}$$

with the same flux limiter function.

In addition to the aforementioned methods, the size-independent high-resolution method (Eq. 5) can be extended to simulate the PBE with size-dependent growth. Assuming that the growth rate does not depend on time, multiplying Eq. 9 by G gives

$$\frac{\partial (Gf)}{\partial t} + G\,\frac{\partial (Gf)}{\partial L} = 0 \tag{12}$$

Defining $\tilde{f} = Gf$, and rewriting Eq. 12 in terms of $\tilde{f}$ gives

$$\frac{\partial \tilde{f}}{\partial t} + G\,\frac{\partial \tilde{f}}{\partial L} = 0 \tag{13}$$

which, *for each grid point*, is equivalent to the population balance equation for size-independent growth (Eq. 4). The high-resolution algorithm for size-independent growth can be used for simulating $\tilde{f}$ with the constant growth rate g in Eq. 5, replaced by the size-dependent growth rates evaluated at the grid midpoints

$$\text{HR3:}\quad \tilde{f}_n^{m+1} = \tilde{f}_n^m - \frac{kG_{n-1/2}}{h}(\tilde{f}_n^m - \tilde{f}_{n-1}^m) - \left[\frac{kG_{n+1/2}}{2h}\left(1 - \frac{kG_{n+1/2}}{h}\right)(\tilde{f}_{n+1}^m - \tilde{f}_n^m)\phi_n - \frac{kG_{n-1/2}}{2h}\left(1 - \frac{kG_{n-1/2}}{h}\right)(\tilde{f}_n^m - \tilde{f}_{n-1}^m)\phi_{n-1}\right] \quad (14)$$

The flux limiter function $\phi(\tilde{\theta})$ uses the same functionality as in Eq. 8, with the measure of smoothness given by

$$\tilde{\theta}_n = \frac{\tilde{f}_n^m - \tilde{f}_{n-1}^m}{\tilde{f}_{n+1}^m - \tilde{f}_n^m} \quad (15)$$

The true distribution f is then computed from the distribution $\tilde{f}$ using

$$f_n^m = \frac{\tilde{f}_n^m}{G_n} \quad (16)$$

The HR3 algorithm is not second-order accurate even without the limiters, but in practice this algorithm often gives comparable accuracy to the HR1 method (see Example 1 in the section entitled Numerical Examples). For each high-resolution algorithm, there exists a corresponding upwind method and modified Lax-Wendroff scheme, which are obtained by setting the flux limiter function ϕ to zero and one, respectively. However, the modified Lax-Wendroff schemes are not necessarily second-order accurate, except for HR1. The upwind methods from HR2 and HR3 are equivalent provided that G is nonzero for the crystal sizes of interest.

Multiple dimensions and the nonhomogeneous term

In general, the distribution may have multiple internal coordinates, which results in the multidimensional population balance equation

$$\frac{\partial f}{\partial t} + \sum_{j=1}^{n} \frac{\partial\{G_j(L_j) f\}}{\partial L_j} = h(\mathbf{L}, t, f) \quad (17)$$

where G_j is the growth rate along the L_j internal coordinate and $\boldsymbol{L}$ denotes the vector of internal coordinates. These coordinates can also include spatial coordinates, in which case the G_j is the velocity in the direction of the corresponding spatial coordinate. Simulation of the multidimensional population balance equation involves applying the high-resolution algorithm to the homogeneous system

$$\frac{\partial f}{\partial t} + \sum_{j=1}^{n} \frac{\partial\{G_j(\mathbf{L}) f\}}{\partial L_j} = 0 \quad (18)$$

This step consists of applying the 1-D high-resolution algorithm to each 1-D homogeneous system resulting from setting all $G_j = 0$ except for one internal coordinate sequentially at each time instant. This technique is known as *dimensional splitting* (Ma et al., 2002; LeVeque et al., 1998). It is straightforward to extend the numerical analysis of LeVeque et al., 1998, to show that the above high-resolution method with dimensional splitting is second-order accurate for Eq. 17.

After each high resolution step, the nonhomogeneous term $h(\mathbf{L},t,f)$ is added to the distribution function f at each time step—a technique known as a *Godunov splitting*. This method is second-order accurate except for the first and last time steps, which provides accuracy indistinguishable from Strang splitting which is formally second-order accurate for all time steps (LeVeque et al., 1998). The reader is referred to the above references for detailed numerical analyses of the accuracy of these splitting techniques.

Implementation: boundary conditions, zero growth rate, dependencies on time-varying variables, and numerical stability and cost

In the high-resolution algorithms described here, the computation of f_n^{m+1} depends on the values of f_{n-2}^{m}. It is common to assume that sufficiently small entities have essentially zero size (Hounslow, 1990; Hounslow et al., 1988; van Peborgh Gooch and Hounslow, 1996). As the population density at zero size for the next time step requires the current value at size $-h$ and $-2h$, our implementation uses fictitious points at these sizes that have population densities of zero at all times. At the other end, the computation of f_N^{m+1} assumes that f_N^{m+1} for all m, which is known as the absorbing boundary condition (LeVeque, 2002). In many problems, the nonhomogeneous terms depend on the crystal-size distribution and the maximum discretization point N is selected to include the entire distribution.

The transformation in deriving HR3 cannot be applied at discretized points where the growth rates are zero. At these points, the homogeneous PBE is rewritten as

$$\frac{\partial f(\hat{L}, t)}{\partial t} + G(\hat{L})\frac{\partial f(\hat{L}, t)}{\partial L} + f(\hat{L}, t)\frac{\partial G(\hat{L})}{\partial L} = 0 \quad (19)$$

where $G(\hat{L}) = 0$. The second term on the lefthand side drops out, and finite difference approximation gives the density function at the next time step as

$$f_{\hat{n}}^{m+1} = f_{\hat{n}}^m - f_{\hat{n}}^m \left.\frac{\partial G}{\partial L}\right|_{L=\hat{n}h} \quad (20)$$

The derivative on the righthand side can be computed from direct differentiation of the growth function, or can be estimated using finite difference approximation.

In many cases, it is necessary to model the growth rate as a function of time or other time-varying variables, such as temperature or solute concentration. When the growth rate is size-independent, but time-varying, the numerical algorithm is the same as for the population balance Eq. 4, but with $g = g(t)$. That is, the same high-resolution algorithm applies for this problem with the constant g replaced by g^m to reflect the dependence on time. The same modifications also apply to the HR1 and HR2 algorithms (Eqs. 10 and 11).

If the growth rate is a function of both size and a time-

varying variable $z(t)$, then a similar transformation that led Eq. 9 to 12 in HR3 gives

$$\frac{\partial(G(L, z(t))f)}{\partial t} + G(L, z(t))\frac{\partial(G(L, z(t))f)}{\partial L} = f\frac{\partial(G(L, z(t))}{\partial z}\frac{dz(t)}{dt} \quad (21)$$

The resulting nonhomogeneous system can be simulated using the high-resolution algorithm for size-dependent growth rate with $\tilde{f} = G(L, z(t))f$, and the addition of the original nonhomogeneous term and the righthand side of Eq. 21. A simpler expression can be derived for the typical functionality

$$G(L, z(t)) = G_z(z(t))G_L(L) \quad (22)$$

Then, multiplying the original homogeneous population balance equation with only the G_L term and factoring out G_z from the derivative with respect to length gives the homogeneous equation

$$\frac{\partial(G_L f)}{\partial t} + G(L, z(t))\frac{\partial(G_L f)}{\partial L} = 0 \quad (23)$$

As before, the high-resolution algorithm (Eq. 14) can be used to simulation this equation, with $\tilde{f} = G_L f$.

The Courant-Friedrichs-Levy (CFL) condition for size-dependent growth is

$$\left|(\max_n G_n)\frac{k}{h}\right| \leq 1, \quad (24)$$

which is the necessary condition for the convergence of the high-resolution method, as it is necessary for any explicit numerical method. Typically, the mesh size h is fixed, and the CFL condition is rearranged to compute a time interval k, that is further reduced to improve numerical accuracy with respect to the time discretization.

For the same grid, the computational cost of the high-resolution algorithms is approximately twice the cost of the Lax-Wendroff method. The higher accuracy of the high-resolution methods for sharp distributions, however, enables the use of much larger mesh sizes to achieve the same overall level of numerical accuracy. Using a larger mesh size both reduces the number of grid cells for the same size domain and increases the allowable time-step to maintain numerical stability (see Eq. 24). Thus, for the same level of numerical accuracy, the high-resolution algorithms have much lower computational cost than the upwind and Lax-Wendroff methods, especially for multidimensional systems. For example, in Example 2 below the high-resolution algorithm is more numerically accurate than simulation using the Lax-Wendroff method applied to an order-of-magnitude smaller grid cell size. The CFL condition (Eq. 24) indicates that the high-resolution algorithm could use an order-of-magnitude larger time-step, in which case the computational time of the high-resolution method would be a factor of $\sim$ 50 faster than the Lax-Wendroff method. For a 2-D population balance equation, the high-resolution algorithm would be 500$\times$ faster. The memory requirements for the upwind, Lax-Wendroff, and high-resolution methods are the same.

The high-resolution algorithms, which solve the general 1-D and multidimensional population balance Eqs. 1 and 17, are implemented in the ParticleSolver software, which is freely available for use as a stand-alone code, or for incorporation into more complicated process simulations (Gunawan et al., 2003).

Numerical Examples

These examples compare the numerical accuracy and stability with established algorithms.

Example 1: Size-dependent growth in a batch process

This example illustrates the differences among the three high-resolution algorithms for simulating PBEs with size-dependent growth. Consider a batch process with a growth rate that depends linearly on mass

$$G(v) = G_0 v \quad (25)$$

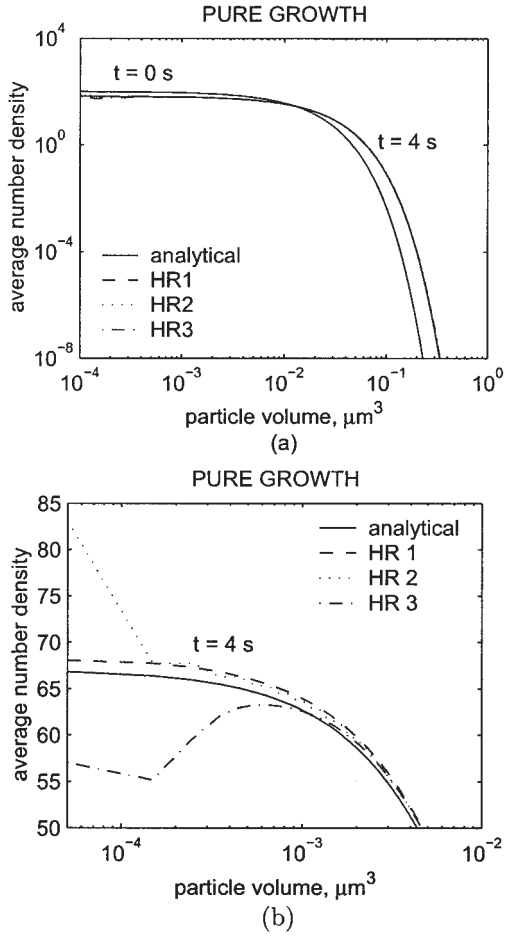

Figure 1. Analytical and numerical distributions using the high-resolution methods (10), (11), and (14), shown here as HR 1, HR 2, and HR 3, respectively (Example 1).

Table 1. Simulation Parameters in Example 1

Variable	Description	Value	Units
k	Time interval	10^{-4}	s
h	Mesh size	10^{-4}	μm^3
v_0	Mean volume of charge	0.01	μm^3
N_0	Number of crystals in v_0	1	Dimensionless
G_0	Growth rate	0.1	$\mu m^3/s$

where G_0 is a constant and the initial distribution is

$$f(v, 0) = \frac{N_0}{v_0} e^{-v/v_0} \tag{26}$$

where v_0 is the mean volume of the charge and N_0 is the total initial number of particles in v_0. The analytical solution is (Kumar and Ramkrishna, 1997; Ramabhadran et al., 1976)

$$f(v, t) = \frac{N_0}{v_0} \exp\left[-\frac{v}{v_0} e^{-G_0 t} - G_0 t \right] \tag{27}$$

Figure 1 compares the simulated CSDs from the three high-resolution algorithms using the simulation parameters listed in Table 1. Table 2 presents the average and the maximum absolute errors associated with each method. While the average absolute error is similar for the three high-resolution methods, the maximum absolute error and Figure 1b indicate that HR1, which is formally second-order accurate without limiter, provided the best agreement with the analytical distribution. The larger deviations at the smaller size range arise from using the boundary condition at zero volume as described earlier, which is numerically equivalent to having a discontinuity at zero size. In this case, the HR1 was able to keep the propagation of the boundary condition error much lower than the HR2 and HR3 methods. The remaining examples in this section will use HR1 as the high-resolution algorithm for simulating PBEs with size-dependent growth rates.

Example 2: Nucleation and size- and concentration-dependent growth in a batch process

This example illustrates the accuracy of the high-resolution algorithm for a batch process with nucleation and growth, where the growth rate is a function of size and time-varying variables; in this case, the solution concentration and temperature

$$\frac{\partial f(L, t)}{\partial t} + \frac{\partial \{G(L, c(t), T(t)) f(L, t))\}}{\partial L} = B_0(c(t), T(t))\delta(L) \tag{28}$$

Table 2. Average and Maximum Absolute Error (Example 1)

Method	Avg. Abs. Error	Max. Abs. Error
HR1	2.0×10^{-2}	1.37
HR2	2.0×10^{-2}	16.3
HR3	2.1×10^{-2}	11.2

Table 3. Kinetic Parameters (Example 2)

Variable	Value	Units
b	1.78	Dimensionless
k_b	4.64×10^{-7}	particles/μm^3/s
g	1.32	Dimensionless
k_g	1.16×10^{2}	μm/s

where c is the solution concentration, B_0 is the rate of nucleation of particles of zero size (Hounslow, 1990; Hounslow et al., 1988; van Peborgh Gooch and Hounslow, 1996), and δ is the dirac delta function. For a seeded batch crystallization, the dominant mechanism of crystal birth is secondary nucleation, and the nucleation kinetics are typically in power-law form (Nyvlt et al., 1985; Randolph and Larson, 1988)

$$B_0(c, T) = k_b V \left(\frac{c - c_{sat}(T)}{c_{sat}(T)} \right)^b \tag{29}$$

where k_b and b are the kinetic parameters, V is the total volume of crystals in the system, and c_{sat} denotes the saturated solute concentration (the time-dependence in c and T are suppressed to simplify notation). The growth rate has linear size-dependence and a similar power law functionality

$$G(L, c, T) = k_g \left(\frac{c - c_{sat}(T)}{c_{sat}(T)} \right)^g (1 + 0.1L) \tag{30}$$

where k_g and g are the kinetic parameters. The kinetic parameters reported for the crystallization of potassium nitrate (KNO3) crystals were used (see Table 3). The solution concentration obeys the mass balance

$$\frac{dc}{dt} = -3\rho_c \int_0^\infty GfL^2 dL \tag{31}$$

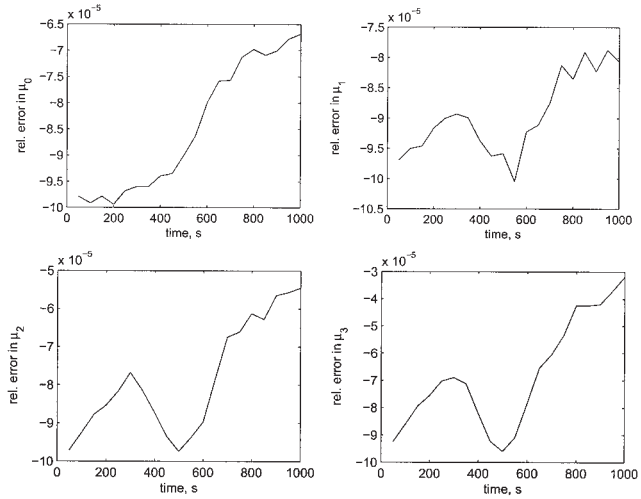

Figure 2. Relative error in moments 0, 1, 2, and 3 predictions using the high-resolution method for a batch process with size-and concentration-dependent growth rate (Example 2).

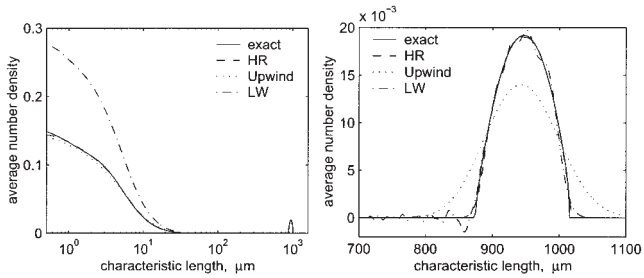

Figure 3. Crystal-size distributions from the high resolution (HR), the upwind, and the Lax-Wendroff (LW) methods using moderate size interval with the "exact" density function at t = 1,000 s (Example 2).

where ρ_c is the crystal density ($\rho_c = 2.11 \times 10^{-12}$ g/μm^3), and the saturated solution concentration is (Miller, 1993)

$$c_{sat}(T)\ [\text{g/g of water}] = 1.721 \times 10^{-4}T^2 - 5.88 \times 10^{-3}T + 0.1286 \quad (32)$$

The simulation used an exponentially decaying temperature trajectory

$$T(t)\ [^\circ\text{C}] = 32 - 4(1 - e^{-t/18600}) \quad (33)$$

There exists no analytical solution to Eq. 28, so a high resolution simulation using a very fine mesh size provided the "exact" CSD, whose numerical accuracy was confirmed using the method of moments (Hulburt and Katz, 1964). The initial moments were evaluated analytically for the initial distribution

$$f(L, 0) = \begin{cases} -3.48 \times 10^{-4}L^2 + 0.136L - 13.3 \\ \quad \text{if } 180.5\ \mu\text{m} \le L \le 210.5\ \mu\text{m} \\ 0 \quad \text{elsewhere} \end{cases} \quad (34)$$

As shown in Figure 2, the zeroth through third moments from the "exact" high-resolution simulation ($k = 10^{-2}$s, $h = 0.05$ μm, $N = 32{,}000$) agree very well with those obtained using the method of moments. Figure 3 compares the CSDs from the high-resolution, the upwind, and the Lax-Wendroff methods using a moderate size interval ($h = 0.5$ μm, $N = 3{,}200$) with the "exact" CSD computed earlier. The average absolute error for the different methods is reported in Table 4, which shows that the high-resolution method was an order of magnitude more accurate than the upwind and the Lax-Wendroff methods. The inaccuracies in the upwind method were caused by numerical diffusion, which was apparent in Figure 3b. The error in the Lax-Wendroff method arised from numerical dispersion associated with the antidiffusion term, which induced nonphysical generation of small crystals (see Figure 3a) and spurious

Table 4. Average Absolute Error (Example 2)

Methods	Avg. Abs. Error
High res.	3.21×10^{-5}
Upwind	5.44×10^{-4}
Lax-Wendroff	5.75×10^{-4}

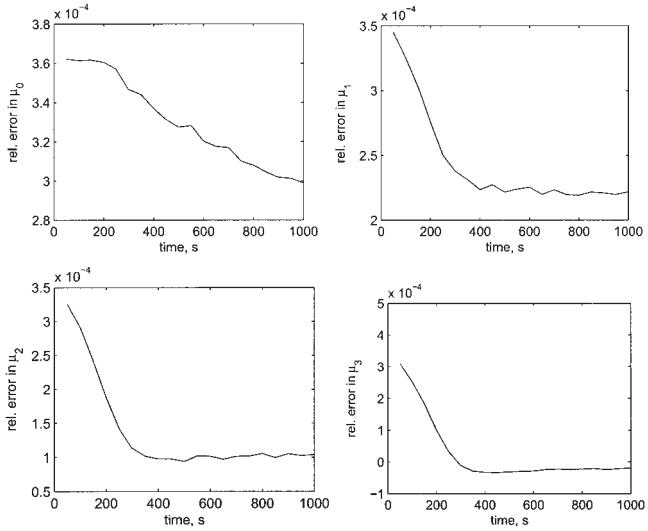

Figure 4. Relative error in moments 0, 1, 2, and 3 predictions using the high-resolution method for a batch process with size-independent and concentration-dependent growth rate (Example 2).

oscillations (see Figure 3b). The high-resolution algorithm provided a much more accurate CSD without significant numerical diffusion or dispersion.

Additional simulations compare the accuracy of the high resolution, the upwind, and the Lax-Wendroff methods for size-independent and size-dependent growth for different mesh sizes. This is to elucidate whether the technique used to address size-dependent growth affects the numerical accuracy or the selection of numerical parameters in the simulation algorithms.

In these simulations, the size-dependent growth rate was the same as earlier, and the size-independent growth rate was

$$G(c, T) = k_g\left(\frac{c - c_{sat}}{c_{sat}}\right)^g (\max_L (1 + 0.1L)) \quad (35)$$

such that the CFL condition for the two growth rates are equivalent. Figure 4 shows the agreement in the moments computed using the method of moments and the high resolution method with fine interval sizes ($k = 10^{-2}$s, $h = 0.05$ μm, $N = 32{,}000$), which provides the "exact" CSD for the size-independent growth rate. Two mesh sizes were considered ($h = 0.1$ μm and $h = 1$ μm). The average absolute error in the CSDs from the high resolution, the upwind, and the Lax-Wendroff simulations is reported in Table 5, and the corresponding CSDs are shown in Figures 5, 6, and 7. Comparison of the error suggests that the size-dependency of the growth rate does not necessitate higher computational requirements than the size-independent

Table 5. Average Absolute Error for Size-Dependent and Size-Independent Growth Rates (Example 2)

	Avg. Abs. Error $h = 0.1$ μm ($h = 1$ μm)	
Methods	Size Dep.	Size Indep.
High res.	3.65×10^{-6} (7.68×10^{-5})	8.36×10^{-6} (1.72×10^{-4})
Upwind	1.50×10^{-4} (8.40×10^{-4})	4.60×10^{-4} (1.43×10^{-3})
Lax-Wendroff	5.56×10^{-4} (6.13×10^{-4})	2.89×10^{-4} (9.42×10^{-4})

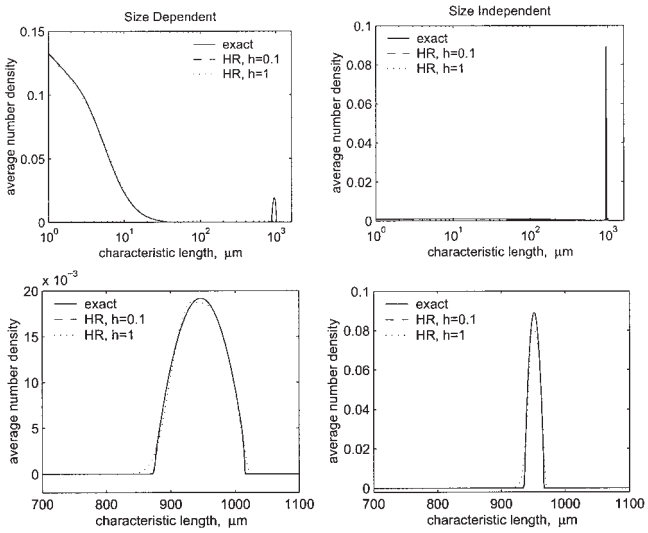

Figure 5. Crystal-size distributions from the high-resolution algorithms for size-independent and size-dependent growth rates with mesh sizes $h = 1$ μm and $h = 0.1$ μm (Example 2).

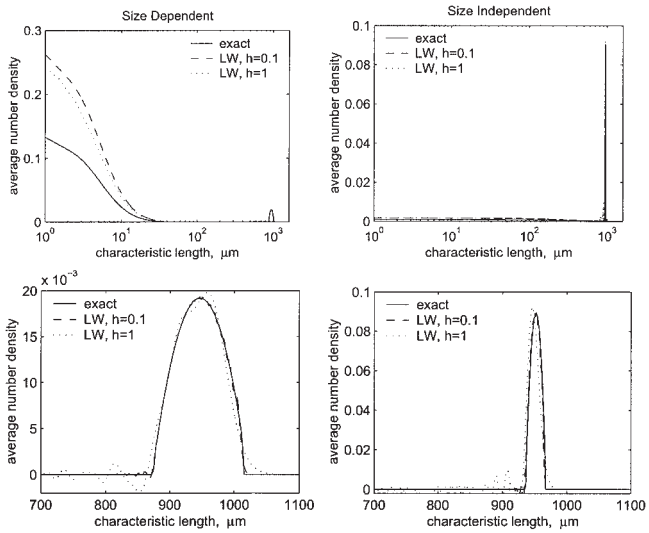

Figure 7. Crystal-size distributions from the Lax-Wendroff method for size-independent and size-dependent growth rates with mesh sizes $h = 1$ μm and $h = 0.1$ μm (Example 2).

growth rate. Again, the high-resolution algorithms gave much more accurate simulations compared to the upwind and the Lax-Wendroff methods. Moreover, the errors also indicate that the high resolution algorithm achieved higher accuracy than the upwind and Lax-Wendroff methods with an order of magnitude larger grid cell size.

Example 3: Nucleation and size-and concentration-dependent growth in a multidimensional batch process

This example illustrates the ability of the high-resolution algorithms to accurately simulate multidimensional population balance equations. A batch crystallization model that describes the temporal evolution of the distribution as a function of the two main growth axes of potassium dihydrogen-phosphate (KDP) is

$$\frac{\partial f(L_1, L_2, t)}{\partial t} + \frac{\partial\{G_1(L_1, L_2, c, T) f\}}{\partial L_1} + \frac{\partial\{G_2(L_1, L_2, c, T) f\}}{\partial L_2} = B_0(c, T)\delta(L_1)\delta(L_2) \quad (36)$$

where L_1 and L_2 are the characteristic crystal lengths (see, Figure 8), and the dependence of c and T on time is suppressed to simplify notation. The growth rates G_1 and G_2 are assumed to follow a similar power law function of the supersaturation as in Example 2

$$G_1(L_1, L_2, c, T) = k_{g_1}\left(\frac{c - c_{sat}(T)}{c_{sat}(T)}\right)^{g_1} 0.1(1 + 0.6L_1) \quad (37)$$

$$G_2(L_1, L_2, c, T) = k_{g_2}\left(\frac{c - c_{sat}(T)}{c_{sat}(T)}\right)^{g_2} 0.1(1 + 0.6L_2) \quad (38)$$

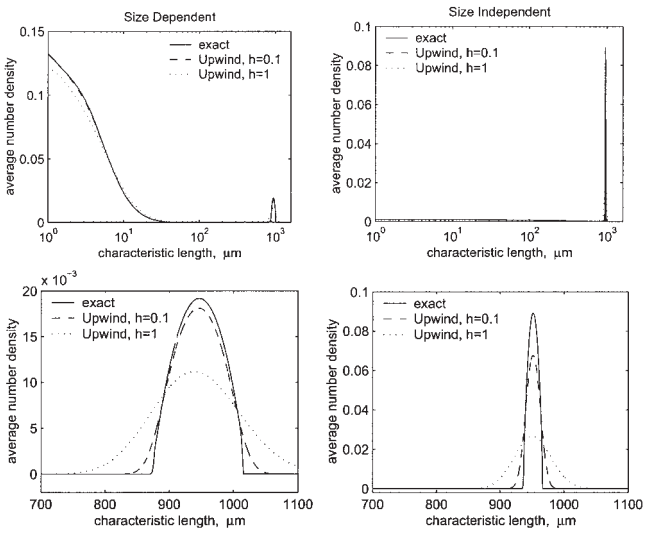

Figure 6. Crystal-size distributions from the upwind scheme for size-independent and size-dependent growth rates with mesh sizes $h = 1$ μm and $h = 0.1$ μm (Example 2).

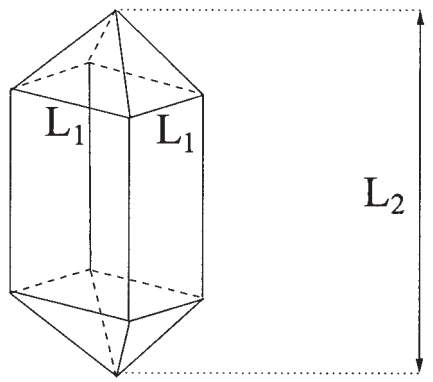

Figure 8. Characteristic lengths of KDP crystals.

Table 6. Kinetic Parameters (Example 3)

Variable	Value	Units
b	2.04	Dimensionless
k_b	7.49×10^{-8}	particles/μm^3/s
g_1	1.48	Dimensionless
k_{g_1}	12.1	μm/s
g_2	1.74	Dimensionless
k_{g_2}	100.75	μm/s

where k_{g1}, k_{g2}, g_1, and g_2 are the kinetic parameters. The nucleation kinetics $B_0(c,T)$ are the same as in Example 2. The temperature trajectory $T(t)$ follows a similar exponential decaying profile

$$T(t)\ [^\circ\text{C}] = 32 - 4(1 - e^{-t/310}) \tag{39}$$

The kinetic parameters determined from experimental data (Gunawan et al., 2002) are reported in Table 6. The solution concentration is given by the solute mass balance

$$\frac{dc}{dt} = -\rho_c \int_0^\infty \int_0^\infty f(L_1, L_2, t)(2G_1(L_1L_2 - L_1^2) + G_2L_1^2)dL_1dL_2 \tag{40}$$

where the crystal density $\rho_c = 2.338 \times 10^{-12}$ g/μm^3, and the saturated solution concentration obeys (Togkalidou et al., 2001)

$$c_{sat}(T)\ [\text{g/g of water}] = 9.3027 \times 10^{-5}T^2 - 9.7629 \times 10^{-5}T + 0.2087 \tag{41}$$

There is no analytical solution to Eq. 36, so a high resolution simulation using a small interval sizes was used as the "exact" CSD, whose accuracy was confirmed by comparison to the method of moments. The simulations used the initial distribution

$$f(L_1, L_2, 0) = \begin{cases} -3.48 \times 10^{-4}(L_1^2 + L_2^2) + 0.136(L_1 + L_2) - 26.6 \\ \quad \text{if } 180.5\ \mu\text{m} \le L_1, L_2 \le 210.5\ \mu\text{m} \\ 0 \quad \text{elsewhere} \end{cases} \tag{42}$$

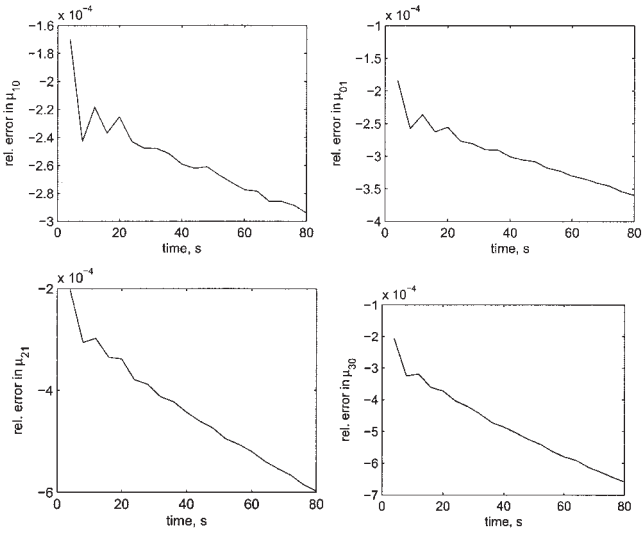

Figure 9. Relative error in moments 10, 01, 21, and 30 predictions using the high-resolution method for a 2-D batch crystallizer of KDP (Example 3).

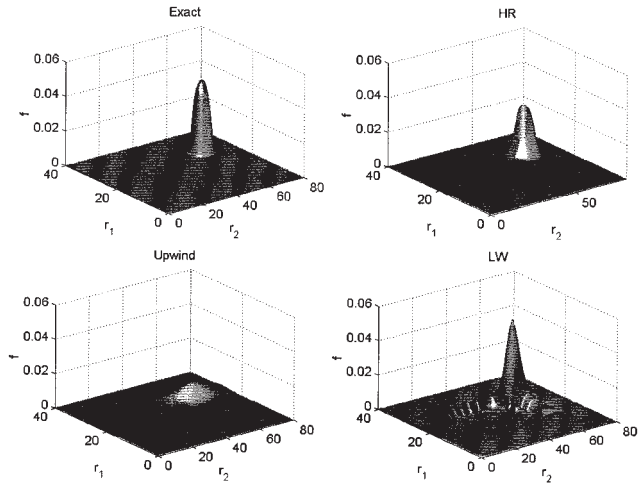

Figure 10. Crystal-size distributions from the high-resolution (HR), the upwind, and the Lax-Wendroff (LW) methods using moderate size interval with the "exact" density function at t = 80 s (Example 3).

Figure 9 shows that the moments from the "exact" CSD using the high-resolution algorithm (k = 0.01 s, $h_1 = h_2 = 0.1$ μm, $N_1 = 600$, $N_2 = 2000$) and the moment of methods agreed very well. Figure 10 compares the simulated CSDs using the high-resolution, the upwind, and the Lax-Wendroff algorithms with moderate interval sizes ($h_1 = h_2 = 0.5$ μm, $N_1 = 120$,$N_2 = 400$) with the "exact" CSD. Table 7 reports the average absolute error in the simulated CSDs.

From inspection of Figure 10, it is clear that the CSD from the high-resolution method is much more accurate qualitatively and quantitatively than the Lax-Wendroff and upwind methods. The numerical diffusion of the upwind method is much more extensive than the high resolution method. The Lax-Wendroff method simulates the region near the maximum value of the CSD quite well, but numerical dispersion induced spurious 2-D oscillations.

Example 4: Nucleation and size-dependent growth in a continuous process.

This numerical example illustrates the accuracy of the high-resolution algorithms for population balance equations for con-

Table 7. Average Absolute Error (Example 3)

Methods	Avg. Abs. Error
High res.	1.2×10^{-4}
Upwind	3.2×10^{-4}
Lax-Wendroff	5.0×10^{-4}

Table 8. Simulation Parameters for Size-Independent Growth Rate in an MSMPR Crystallizer (Examples 4 and 5)

Variable	Description	Value	Units
k	Time interval	0.01	s
h	Mesh size	0.01	μm
L_0	(mean volume of charge)$^{1/3}$	1	μm
G_0	Growth rate	0.00168	μm/s
B_0	Nucleation rate	2×10^{-10}	$\mu m^{-3}\ s^{-1}$
τ	Residence time	100	s

tinuous processes with nucleation and size-dependent growth. The dynamic population balance equation for simultaneous nucleation and growth in a mixed suspension mixed product removal (MSMPR) process is (van Peborgh Gooch and Hounslow, 1996)

$$\frac{\partial f}{\partial t} + \frac{\partial (G(L) f(L))}{\partial L} = B_0 \delta(L) - \frac{f(L)}{\tau} \tag{43}$$

where τ is the residence time in the crystallizer.

The most widely used equation for modeling size-dependent growth is the Abegg-Stevens-Larson (ASL) equation

$$G(L) = G_0(1 + \gamma L)^z \qquad z < 1,\ L \geq 0 \tag{44}$$

where G_0, γ, and z are constants. For the ASL growth function, the steady-state solution of the MSMPR population balance Eq. 43 is (van Peborgh Gooch and Hounslow, 1996)

$$\lim_{t \to \infty} f(L) = \frac{B_0}{G_0} (1 + \gamma L)^{-z} \exp\left(\frac{1 - (1 + \gamma L)^{1-z}}{G_0 \tau \gamma (1 - z)} \right). \tag{45}$$

To compare the numerical results with the analytical solution, Eq. 43 was simulated for long times using the analytical distribution (Eq. 45) as the initial condition, and the parameters

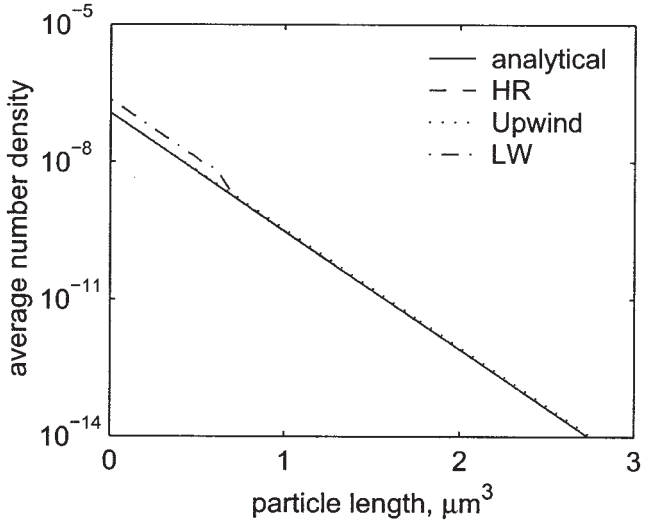

Figure 11. Analytical and numerical distributions for size-independent growth rate ($z = 0$ in Eq. 44) in a MSMPR crystallizer (Example 4).

The analytical and high-resolution distributions overlap.

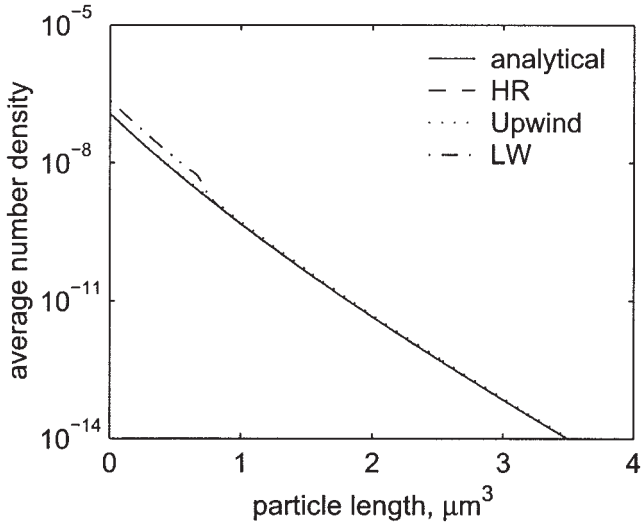

Figure 12. Analytical and numerical distributions for size-dependent growth rate ($z = 0.3, \gamma = 1$) in an MSMPR crystallizer (Example 4).

The analytical and high resolution distributions overlap.

in Table 8. Note that this is not a particularly fine mesh size for simulating a population balance equation. Figures 11 and 12 show the distributions at times $t = 0$ s and $t = 400$ s for size-independent and size-dependent growth rates, respectively. Even for a long time there are negligible numerical diffusion and dispersion of the distributions for either growth rates for the high-resolution method. Table 9 compares the average absolute error in the simulations for the high-resolution, the upwind, and the Lax-Wendroff methods. The high-resolution algorithms again gave the most accurate simulations, which were an order of magnitude more accurate than the upwind and two-orders of magnitude more accurate than the Lax-Wendroff. The upwind method gave less accurate simulations due to numerical diffusion which slightly flattened the distribution, while the Lax-Wendroff method gave significant deviations at small size ranges due to nonphysical generation of small crystals from numerical dispersion (see Figure 11).

Example 5: Step and spike perturbations in a continuous process

This example investigates the behavior of the algorithms when step and spike perturbations are introduced to the steady-state distribution (Eq. 45) with size-dependent growth rate, as in Figure 12, and the evolution of the perturbed distributions are simulated according to Eq. 43. Figures 13 and 14 present the simulation results for step-up and step-down perturbations, respectively, with the simulation parameters reported in Table 8. The perturbed distributions converge to the steady-state

Table 9. Average Absolute Error (Example 4)

	Avg. Abs. Error	
Methods	Size Indep.	Size Dep.
High res.	3.97×10^{-12}	4.15×10^{-12}
Upwind	2.13×10^{-11}	2.18×10^{-11}
Lax-Wendroff	9.22×10^{-10}	9.19×10^{-10}

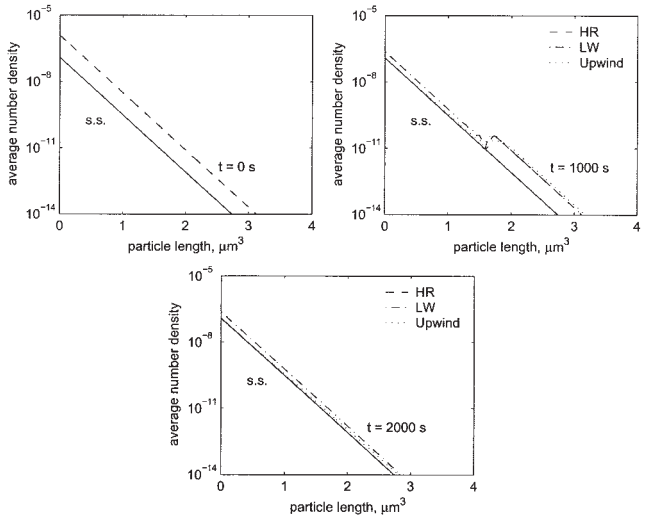

Figure 13. Return of the distribution to the MSMPR steady-state (s.s.) distribution after a step-up perturbation using the high-resolution (HR), the Lax-Wendroff (LW), and the upwind methods (Example 5).

MSMPR distribution with negligible numerical diffusion or dispersion. As in Example 4, the high-resolution gave the highest accuracy followed by the upwind and Lax-Wendroff methods, respectively. The magnitude of the step perturbation affects the time needed to go back to the steady-state distribution, but not the final distribution that each method converges to.

A spike disturbance in the distribution is particularly challenging to handle, and was used to compare numerical results with the popular upwind and Lax-Wendroff methods. Using the simulation parameters listed in Table 8, Figure 15 shows

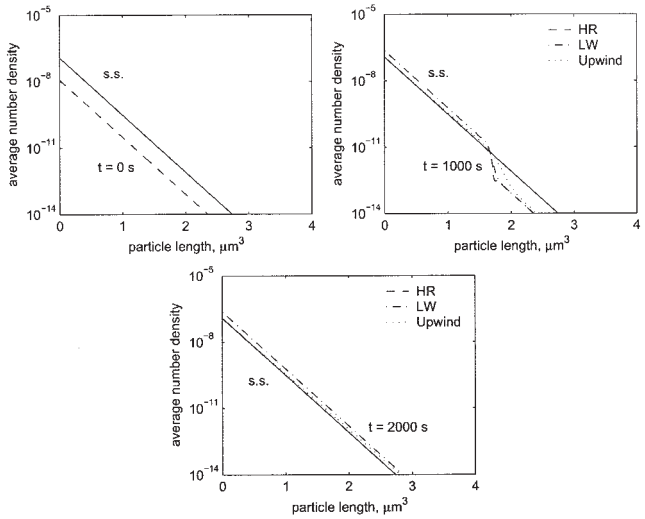

Figure 14. Return of the distribution to the MSMPR steady-state (s.s.) distribution after a step-down perturbation using the high-resolution (HR), the Lax-Wendroff (LW), and the upwind methods (Example 5).

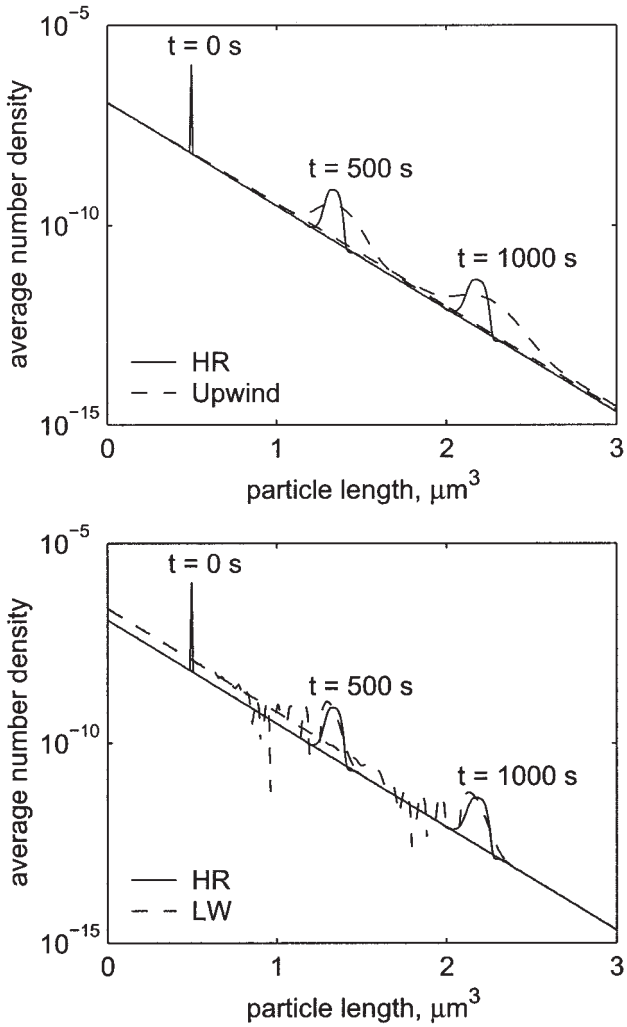

Figure 15. High-resolution, the upwind, and the Lax-Wendroff simulations for a spike perturbation (Example 5).

how the spike moves from smaller to larger sizes (that is, left to right) with time due to crystal growth, while the spike's width increases and height decreases as the distribution evolves to the steady-state distribution. The high-resolution method produces much less numerical diffusion than the upwind method, and much less numerical dispersion than the Lax-Wendroff method.

Conclusions

High-resolution finite volume algorithms were introduced and extended to simulate 1-D and multidimensional population balance equations with nucleation and size-dependent growth. The algorithms avoid the numerical diffusion associated with first-order methods, and the numerical dispersion associated with other second-order methods near discontinuities or sharp gradients. The high-resolution algorithms gave consistent and accurate simulation results for batch and continuous population balance models with a variety of initial conditions. For sharp distributions, the improved numerical accuracy of the high-resolution algorithms enables the use of larger mesh sizes and

longer time steps, resulting in orders-of-magnitude reduction in computational cost compared to alternative finite difference/finite volume methods, while providing similar overall numerical accuracy. All of the high resolution algorithms in this article, which solve the general population balance Eqs. 1 and 17, are implemented in the ParticleSolver software, which is freely available for use as a stand-alone code, or for incorporation into more complicated process simulations (Gunawan et al., 2003).

Literature Cited

Gelbard, F., Y. Tambour, and J. H. Seinfeld, "Sectional Representations for Simulating Aerosol Dynamics," *J. of Colloid and Interface Sci.*, **76**, 541 (1980).

Gunawan, R., I. Fusman, and R. D. Braatz, "ParticleSolver," computer software, available at http://brahms.scs.uiuc.edu (2003).

Gunawan, R., D. L. Ma, M. Fujiwara, and R. D. Braatz, "Identification of Kinetic Parameters in a Multidimensional Crystallization Process," *Int. J. Mod. Phys. B*, **16**, 367 (2002).

Hounslow, M. J., "A Discretized Population Balance for Continous Systems at Steady-State," *AIChE J.*, **36**, 106 (1990).

Hounslow, M. J., R. L. Ryall, and V. R. Marshall, "A Discretized Population Balance for Nucleation, Growth, and Aggregation," *AIChE J.*, **34**, 1821 (1988).

Hulburt, H. M., and S. Katz, "Some Problems in Particle Technology," *Chem. Eng. Sci.*, **19**, 555 (1964).

Kumar, S., and D. Ramkrishna, "On the Solution of Population Balance Equations by Discretization -I. a Fixed Pivot Technique," *Chem. Eng. Sci.*, **51**, 1311 (1996).

Kumar, S., and D. Ramkrishna, "On the Solution of Population Balance Equations by Discretization -III. Nucleation, Growth and Aggregation of Particles," *Chem. Eng. Sci.*, **52**, 4659 (1997).

LeVeque, R. J., *Numerical Methods for Conservation Laws*, Birkhäuser Verlag, Basel, Germany (1992).

LeVeque, R. J., *Finite Volume Methods for Hyperbolic Problems*, Cambridge Univ. Press, New York, NY (2002).

LeVeque, R. J., D. Mihalas, E. A. Dorfi, and E. Muller, *Computational Methods for Astrophysical Fluid Flow*, Springer-Verlag, Berlin (1998).

Ma, D. L., D. K. Tafti, and R. D. Braatz, "High Resolution Simulation of Multidimensional Crystal Growth," *Ind. Eng. Chem. Res.*, **41**, 6217 (2002).

Maisels, A., F. E. Kruis, and H. Fissan, "Direct Monte Carlo Simulations of Coagulation and Aggregation," *J. of Aerosol Science*, **30**, S417 (1999).

Marchal, P., R. David, J. P. Klein, and J. Villermaux, "Crystallization and Precipitation Engineering. I: An Efficient Method for Solving Population Balance in Crystallization with Agglomeration," *Chem. Eng. Sci.*, **43**, 59 (1988).

Miller, S. M., *Modelling and Quality Control Strategies for Batch Cooling Crystallizers*, PhD Thesis, Univ. of Texas at Austin (1993).

Morton, K. W., and D. F. Mayers, *Numerical Solution of Partial Differential Equations*, Cambridge University Press, Cambridge, UK (1994).

Muhr, H., R. David, J. Villermaux, and P. H. Jezequel, "Crystallization and Precipitation Engineering -VI. Solving Population Balance in the Case of the Precipitation of Silver Bromide Crystals with High Primary Nucleation Rates by using the First Order Upwind Differentiation," *Chem. Eng. Sci.*, **51**, 309 (1996).

Nicmanis, M., and M. J. Hounslow, "Finite-Element Methods for Steady-State Population Balance Equations," *AIChE J.*, **44**, 2258 (1998).

Nyvlt, J., O. Sohnel, M. Matuchova, and M. Broul, *The Kinetics of Industrial Crystallization*, of *Chemical Engineering Monographs*, Elsevier, Amsterdam, Vol. 19 (1985).

Ramabhadran, T. E., T. W. Peterson, and J. H. Seinfeld, "Dynamics of Aerosol Coagulation and Condensation," *AIChE J.*, **22**, 840 (1976).

Ramkrishna, D., "The Status of Population Balances," *Rev. Chem. Eng.*, **3**, 49 (1985).

Ramkrishna, D., *Population Balances: Theory and Applications to Particulate Systems in Engineering*, Academic Press, San Diego, CA (2000).

Randolph, A., and M. A. Larson, *Theory of Particulate Processes*, 2nd ed., Academic Press, San Diego (1988).

Shah, B. H., D. Ramkrishna, and J. D. Borwanker, "Simulation of Particulate Systems Using the Concept of the Interval of Quiescence," *AIChE J.*, **23**, 897 (1977).

Singh, P. N., and D. Ramkrishna, "Solution of Population Balance Equations by MWR," *Comp. & Chem. Eng.*, **1**, 23 (1977).

Song, M., and X. J. Qiu, "Alternative to the Concept of the Interval of Quiescence (IQ) in the Monte Carlo Simulation of Population Balances," *Chem. Eng. Sci.*, **54**, 5711 (1999).

Togkalidou, T., M. Fujiwara, S. Patel, and R. D. Braatz, "Solute Concentration Prediction Using Chemometrics and ATR-FTIR Spectroscopy," *J. Cryst. Growth*, **231**, 534 (2001).

van Leer, B., "Toward the Ultimate Conservative Difference Scheme II. Monotonicity and Conservation Combined in a Second-Order Scheme," *J. Comput. Phys.*, **14**, 361 (1974).

van Peborgh Gooch, J. R., and M. J. Hounslow, "Monte Carlo Simulation of Size-Enlargement Mechanisms in Crystallization," *AIChE J.*, **42**, 1864 (1996).

Manuscript received June 6, 2003, and revision received March 8, 2004.